# Tunable topological defect states and single-quanta skyrmionic configurations in mesoscopic superconducting rectangular systems with spin-orbit interaction

Rui-Feng Chai,[1] Yue Xie [,1] Ling-Feng Zhang,[1,2,*] and Guo-Qiao Zha [1,2,†]

[1]*Department of Physics, Shanghai University, Shanghai 200444, China*
[2]*Shanghai Key Laboratory of High Temperature Superconductors, Shanghai University, Shanghai 200444, China*

In the framework of the microscopic Bogoliubov-de Gennes theory, we investigate the topological defect states under out-of-plane magnetic flux in a mesoscopic superconducting rectangular system with spin-orbit (SO) interaction. The $s + id$ superconducting phase with time-reversal symmetry breaking can be realized by suitable choice of model parameters. For the perfect rectangle with pure Dresselhaus SO interaction, the unclosed domain wall carrying two one-component vortices and double-quanta coreless skyrmions can arise stably with increasing flux. Interestingly, when the admixed Rashba SO coupling is included, the evolution of vortex matter toward the single-quanta coreless skyrmion with unit topological charge $Q = 1$ favors to take place in the present rectangular system. The relative strength of coupled condensates can be effectively tuned by the strengths of Rashba SO coupling and next-nearest-neighbor hopping, giving rise to rich multiple and hybrid topological defect configurations containing even number of $Q = 1$ skyrmions. Moreover, an appropriate in-plane Zeeman potential can drive the splitting of enclosed vortex chains, accompanied with the emergence of obvious single-quanta skyrmionic characters. In particular, the number and location of topological defects are highly sensitive to the surface indentation defect. The single-skyrmionic and multiskyrmionic states consisting of odd number of $Q = 1$ skyrmions can also be produced by introducing a defect in the middle of the short or the long edge of the rectangle. Our investigation may shed new light on the single-quanta skyrmions and provide useful information for observing and tuning topological defect states in multicomponent superconducting systems.

## I. INTRODUCTION

Spin-orbit (SO) interaction is generally used to describe the fundamental coupling mechanism between the spin and orbital degrees of freedom of electrons in solids [1–3]. There are two types of SO interactions, which are so-called Rashba and Dresselhaus SO couplings [4,5]. The Rashba SO coupling arises due to the microscopic structural inversion asymmetry, while the Dresselhaus one is originated from the bulk inversion asymmetry in crystalline structures and the interface inversion asymmetry [6]. In recent years, the emergence of various topological phases in condensed matter systems has drawn a great deal of attention where the SO interaction plays a critical role [2,7,8]. Among them, the topological superconductors with first-order and second-order topological phases are significant as they can host zero-energy Majorana edge and corner modes, which are believed to have great potential applications in topological quantum computations [9–16]. Considering that the search for odd-parity superconducting materials with $p$-wave pairing symmetry, which can provide a natural realization of topological superconductivity, is a challenge, many realistic equivalent routes have been proposed [17–20], such as the system with an even-parity $s$-wave

or $d$-wave superconductor in proximity contact with materials with strong SO coupling.

On the other hand, the novel states of topological defects in superconductors with multicomponent order parameters have attracted tremendous interest recently. The competition between coupled condensates can result in several distinct classes of vortex matter. Nonuniform vortex patterns [21–23] and domain-wall structures separating different chiral states [24–27] can take place in such superconducting systems with broken time-reversal symmetry. Remarkably, a complex coreless vortex state, i.e., the skyrmion with a closed domain wall, can be less energetic than conventional singular-core vortices and become thermodynamically stable in chiral $p + ip$ superconductors [28–32]. Such skyrmionic topological defects do not exhibit singularity in the order-parameter space and can be labeled by nonzero and integer topological charge $Q$ [33,34]. Rich and unique phenomena associated with vortices and skyrmions have also been discussed in $s + is$ and $s + id$ superconducting systems [35–37]. Particularly, the topological defect state can be further stabilized in the presence of mesoscopic edges and its spatial configuration is strongly influenced by the geometric effect [38]. Besides the singly quantized vortex state with a pointlike core, a large number of coreless skyrmionic configurations with $Q \geqslant 2$ are always energetically favored in finite-size superconducting systems containing coexisted pairing orders [39].

Notably, a single-quanta skyrmionic structure with $Q = 1$ is difficult to obtain as a ground state in bulk and finite-size

*lingfeng_zhang@shu.edu.cn
†zgq_1981@shu.edu.cn

*p*-wave superconducting samples. Supported by biquadratic density interactions, a $Q = 1$ chiral skyrmion can remain stable in a superconductor with three bands [40]. Also, a peculiar type of coreless vortices consisting of two spatially separated half-quantum vortices, i.e., the nematic skyrmion with unit topological charge, has been observed in two-component nematic superconductors [41,42]. Especially, unusual vortex configurations can emerge when a mixed *s*- and *d*-wave superconducting order is coupled to the nematic order [43]. Our recent studies have shown that the multiskyrmionic pattern containing several single-quanta skyrmions can be found in mesoscopic superconductors with mixed even-parity pairing symmetries [44]. However, the single-quanta skyrmionic mode consisting of two nonoverlapping half-quantum vortices remains little explored in $s + id$ superconductors up to now. Notice that, for a Rashba superconducting square system, the competition between participating *s*- and *d*-wave condensates can result in unconventional vortex matter [37]. Considering the combination effect of Rashba and Dresselhaus SO couplings [45–47], unique topological defect configurations may be produced in such systems. Additionally, the emergent quantum states in topological superconductors depend strongly on the aspect ratio of fully open systems with SO coupling [48] and can be effectively tuned by applying in-plane Zeeman fields [49]. Particularly, the surface defects can play a pronounced role in vortex penetration in mesoscopic superconductors due to the small size of their boundary [50]. Thus, one may expect that interesting physical phenomena related to skyrmionic states can be present in mesoscopic rectangular superconducting systems with coexisted even-parity pairing.

In view of the above, we provide a careful insight into the topological defect states in a mesoscopic superconducting rectangle with SO interaction by solving the spin-generalized Bogoliubov-de Gennes (BdG) equations [51] in a self-consistent manner. Different from the mesoscopic superconductors with circular and square shapes, an asymmetric rectangular geometry will have a strong impact on properties of samples and novel quantum phenomena may be induced [26]. Based on a tight-binding model Hamiltonian in real space, the even-parity *d*-wave and extended *s*-wave orders can coexist in the present system. The $s + id$ state with broken time-reversal symmetry can be induced by suitable choice of the model parameters. We first examine the evolution of vortex matter under an enlarged out-of-plane flux in the rectangular sample with only the Dresselhaus SO interaction. The single-quanta topological structure with an unclosed domain wall towards sample edges as well as the double-quanta skyrmionic pattern can both appear inside the rectangle. Furthermore, in order to tackle the issue of whether the single-quanta skyrmionic texture can exist in our studied mesoscopic sample, we systematically investigate the effect of admixed Rashba SO interaction on the vortical configurations. Interestingly, when the Rashba SO-coupling strength is increased, unclosed domain-wall state enters the sample, forming the single-quanta coreless skyrmion. Simultaneously, the double-quanta skyrmion can divide into two parts, resulting in stable multiple $Q = 1$ skyrmions. The corresponding spatial profiles of order parameters and zero-energy local density of states (LDOS) as well as the relative phase difference in the order-parameter space are demonstrated. The

next-nearest-neighbor (nnn) hopping effect on order modulations of competing condensates is also discussed. Moreover, we demonstrate that the configurations of topological defects can be effectively tuned by the in-plane Zeeman potential. In particular, the preferable entry position for the vortex is disturbed by the surface defects, and novel spatial patterns of skyrmionic states can be obtained as compared to the perfect mesoscopic sample. We expect that our present results may provide useful information for experiments and futuristic applications in superconducting electronics.

The organization of this paper is as follows. In Sec. II, we introduce the theoretical BdG formalism for a mesoscopic superconducting rectangle with mixed-pairing orders in the presence of SO interactions. In Sec. III, we present the results for different topological defect states in a perfect rectangular system with only the Dresselhaus SO interaction (Sec. III A) and with combined Rashba and Dresselhaus SO couplings (Sec. III B), respectively. We also lay special stress on analyzing the effects of nnn hopping and in-plane Zeeman field on the vortex matter in Sec. III C. In Sec. IV, we discuss the influences of surface defects on the tunable topological defects. Our results are summarized in Sec. V.

## II. MODEL AND FORMULAS

To characterize the property of a two-dimensional (2D) mesoscopic superconducting rectangle in the presence of Rashba and Dresselhaus SO interactions, we start with an effective mean-field Hamiltonian by assuming nearest-neighbor (nn) attraction $V$ for superconducting pairing [11,16]:

$$\hat{H} = \hat{H}_0 + \hat{H}_{\mathrm{Rso}} + \hat{H}_{\mathrm{Dso}}, \tag{1}$$

$$
\hat{H}_0 = -\sum_{\langle \mathbf{ij} \rangle, \sigma} t_{\mathbf{ij}} \exp(i\varphi_{\mathbf{ij}}) c_{\mathbf{i}\sigma}^\dagger c_{\mathbf{j}\sigma} - \mu \sum_{\mathbf{i},\sigma} c_{\mathbf{i}\sigma}^\dagger c_{\mathbf{i}\sigma}
$$
$$
+ \sum_{\langle \mathbf{ij} \rangle} (\Delta_{\mathbf{ij}} c_{\mathbf{i}\uparrow}^\dagger c_{\mathbf{j}\downarrow}^\dagger + \Delta_{\mathbf{ij}}^* c_{\mathbf{j}\downarrow} c_{\mathbf{i}\uparrow})
$$
$$
+ \sum_{\mathbf{i}} [(i\mathbf{h}_y - \mathbf{h}_x) c_{\mathbf{i}\uparrow}^\dagger c_{\mathbf{i}\downarrow} + \mathrm{H.c.}], \tag{2}
$$

$$
\hat{H}_{\mathrm{Rso}} = V_{\mathrm{Rso}} \sum_{\mathbf{i}} [(c_{\mathbf{i}\uparrow}^\dagger c_{\mathbf{i}+\vec{e}_x\downarrow} - c_{\mathbf{i}\downarrow}^\dagger c_{\mathbf{i}+\vec{e}_x\uparrow})
$$
$$
- i(c_{\mathbf{i}\uparrow}^\dagger c_{\mathbf{i}+\vec{e}_y\downarrow} + c_{\mathbf{i}\downarrow}^\dagger c_{\mathbf{i}+\vec{e}_y\uparrow}) + \mathrm{H.c.}], \tag{3}
$$

$$
\hat{H}_{\mathrm{Dso}} = V_{\mathrm{Dso}} \sum_{\mathbf{i}} [(c_{\mathbf{i}\uparrow}^\dagger c_{\mathbf{i}+\vec{e}_y\downarrow} - c_{\mathbf{i}\downarrow}^\dagger c_{\mathbf{i}+\vec{e}_y\uparrow})
$$
$$
- i(c_{\mathbf{i}\uparrow}^\dagger c_{\mathbf{i}+\vec{e}_x\downarrow} + c_{\mathbf{i}\downarrow}^\dagger c_{\mathbf{i}+\vec{e}_x\uparrow}) + \mathrm{H.c.}], \tag{4}
$$

where $t_{\mathbf{ij}} = t$ and $t'$ are the nn and nnn hopping integrals, $c_{\mathbf{i}\sigma}$ ($c_{\mathbf{i}\sigma}^\dagger$) is the destruction (creation) operator for electron of spin $\sigma$ ($\sigma = \uparrow$ or $\downarrow$), and $\vec{e}_{x(y)}$ is the unit vector along the $x$ ($y$) direction. The Peierl's phase factor is given by $\varphi_{\mathbf{ij}} = \pi/\Phi_0 \int_{r_i}^{r_j} \mathbf{A}(\mathbf{r}) \cdot d\mathbf{r}$ with the flux quantum $\Phi_0 = hc/2e$. Here the vector potential $\mathbf{A}(\mathbf{r})$ is chosen the form $H(-y, x, 0)/2$ with magnetic field $H$ in the symmetric gauge, yielding an out-of-plane flux $\Phi$ penetrating the superconductor. $\mu$ is the chemical potential determining the averaged electron density. $\mathbf{h}_y$ ($\mathbf{h}_x$) is the strength of in-plane Zeeman field along the $y$ ($x$) direction, and $V_{\mathrm{Rso}}(V_{\mathrm{Dso}})$ is the Rashba

(Dresselhaus) SO-coupling strength. The superconducting order has the following definition: $\Delta_{ij} = V \langle c_{i\uparrow} c_{j\downarrow} - c_{i\downarrow} c_{j\uparrow} \rangle / 2$. Using the Bogoliubov transformation: $c_{i\uparrow} = \sum_n [u_{i\uparrow}^n \gamma_{n\uparrow} - v_{i\uparrow}^{n*} \gamma_{n\downarrow}^\dagger]$, $c_{i\downarrow} = \sum_n [u_{i\downarrow}^n \gamma_{n\downarrow} + v_{i\downarrow}^{n*} \gamma_{n\uparrow}^\dagger]$, the Hamiltonian in Eq. (1) can be diagonalized by solving the resulting BdG equations self-consistently:

$$\sum_j^N \begin{pmatrix} \mathcal{H}_{ij\uparrow} & V_1 & 0 & \Delta_{ij} \\ V_2 & \mathcal{H}_{ij\downarrow} & \Delta_{ij} & 0 \\ 0 & \Delta_{ij}^* & -\mathcal{H}_{ij\uparrow}^* & V_3 \\ \Delta_{ij}^* & 0 & V_4 & -\mathcal{H}_{ij\downarrow}^* \end{pmatrix} \begin{pmatrix} u_{j\uparrow}^n \\ u_{j\downarrow}^n \\ v_{j\uparrow}^n \\ v_{j\downarrow}^n \end{pmatrix} = E_n \begin{pmatrix} u_{i\uparrow}^n \\ u_{i\downarrow}^n \\ v_{i\uparrow}^n \\ v_{i\downarrow}^n \end{pmatrix},$$

(5)

where $\mathcal{H}_{ij\sigma} = -t_{ij} \exp(i\varphi_{ij}) - \mu \delta_{ij}$, $V_m = V_{Rso}\{[(-1)^{m+1} \delta_{i+\vec{e}_x, j} + (-1)^m \delta_{i-\vec{e}_x, j}] + \lambda_m [i(\delta_{i+\vec{e}_y, j} - \delta_{i-\vec{e}_y, j})]\} + V_{Dso}\{[(-1)^{m+1} \delta_{i+\vec{e}_y, j} + (-1)^m \delta_{i-\vec{e}_y, j}] + \lambda_m [i(\delta_{i+\vec{e}_x, j} - \delta_{i-\vec{e}_x, j})]\} - (-1)^m i\mathbf{h}_y - \mathbf{h}_x$ ($\lambda_m = -1$ for $m = 1, 2$, and $\lambda_m = 1$ for $m = 3, 4$), and $\delta_{i,j}$ represents a delta function. We can get the eigenvalues $\{E_n\}$ with eigenvectors $\{u_\uparrow^n, u_\downarrow^n, v_\uparrow^n, v_\downarrow^n\}$ for the fully open system by introducing open boundary conditions. The order parameter $\Delta_{ij}$ is calculated self-consistently from

$$\Delta_{ij} = \sum_n \frac{V}{4} \left( u_{i\uparrow}^n v_{j\downarrow}^{n*} + u_{j\downarrow}^n v_{i\uparrow}^{n*} + u_{i\downarrow}^n v_{j\uparrow}^{n*} + u_{j\uparrow}^n v_{i\downarrow}^{n*} \right)$$

$$\times \tanh \left( \frac{E_n}{2k_B T} \right).$$

(6)

Then the extended $s$- and $d_{x^2-y^2}$- wave symmetry can be defined, respectively, at site $i$ as

$$\Delta_i^s = \left( \Delta_{i+\vec{e}_x, i}^s + \Delta_{i-\vec{e}_x, i}^s + \Delta_{i, i+\vec{e}_y}^s + \Delta_{i, i-\vec{e}_y}^s \right)/4, \quad (7)$$

$$\Delta_i^d = \left( \Delta_{i+\vec{e}_x, i}^d + \Delta_{i-\vec{e}_x, i}^d - \Delta_{i, i+\vec{e}_y}^d - \Delta_{i, i-\vec{e}_y}^d \right)/4, \quad (8)$$

where $\Delta_{i,j}^s = \Delta_{i,j}^d = \Delta_{ij} \exp[i\pi/\Phi_0 \int_{r_i}^{(r_i+r_j)/2} \mathbf{A}(\mathbf{r})d\mathbf{r}]$. Similar to the studies in the $p_x \pm ip_y$-wave superconducting sample [31,38], the relative phase $\phi_{sd} = \cos(\phi_s - \phi_d)$ between the $s$- and $d$-wave components is defined to display the 2D skyrmionic texture in our system. When the phase difference $(\phi_s - \phi_d) = \pm\pi/2$, $s \pm id$-wave pairings with time-reversal symmetry breaking can arise. Additionally, the topological charge $Q$ for the skyrmion is given by

$$Q = \frac{1}{4\pi} \int \mathbf{n} \cdot (\partial_x \mathbf{n} \times \partial_y \mathbf{n}) dx dy. \quad (9)$$

The three-dimensional pseudospin vector $\mathbf{n}$ is defined as [52]

$$\mathbf{n} = (n_x, n_y, n_z) = \frac{\Delta^\dagger \sigma \Delta}{\Delta^\dagger \Delta}, \quad (10)$$

where the two-component order parameter $\Delta = (\Delta_s, \Delta_d)$ and $\sigma$ is the Pauli matrices.

Note that due to the finite sample with open boundary conditions, the calculated topological charge $Q$ for a skyrmion is not exactly an integer value. Nevertheless, a skyrmion can still be characterized by an integer $Q$, as for a complete skyrmion, the pseudospin texture $\mathbf{n}$ always wraps $Q$ times around a closed surface [31].

To examine the topological defect states in mesoscopic samples, we can calculate the LDOS related to the tunneling conductance in the scanning tunneling microscopic (STM) experiments, which can be written as

$$\rho_i(E) = \sum_{n,\sigma} \left[ |u_{i\sigma}^n|^2 \delta(E_n - E) + |v_{i\sigma}^n|^2 \delta(E_n + E) \right], \quad (11)$$

where the Dirac delta-function $\delta(x)$ is taken as $\Gamma/\pi(x^2 + \Gamma^2)$ with the quasiparticle damping $\Gamma = 0.01$.

Throughout this work, the distance is measured in units of the lattice constant $a$, the magnetic flux in units of $\Phi_0$, and the energy in units of $t$. In the numerical calculations, we take $k_B = a = t = 1$ for simplicity. By choosing an appropriate initial $\Delta_{ij}$, the Hamiltonian is numerically diagonalized and the calculations are repeated until the difference in the order parameters between two consecutive iterations is less than $10^{-6}$. The applied flux as well as the other tunable parameters are slowly increased or decreased with a regular interval to find all the stable solutions. The ground state has the lowest total energy among those of stable states, and then the corresponding evolution of topological defect states can be obtained finally.

## III. TOPOLOGICAL DEFECT STATES IN PERFECT SUPERCONDUCTING RECTANGLES

In the present study, we consider a mesoscopic superconducting rectangle with an outer size of $N_x \times N_y = 24 \times 40$ at zero temperature. In order to generate the mixed-pairing symmetries for the studied lattice system with a nn attractive interaction, the microscopic model parameters are chosen as: the interaction strength $V = 5$ and the chemical potential $\mu = -2$. The SO-coupling effect is introduced into the system, giving rise to a possible $s + id$ superconducting phase [14,16]. In our self-consistent calculations, we fix the strength of Dresselhaus SO interaction $V_{Dso} = 0.3$ and consider that the Rashba SO-coupling strength $V_{Rso}$ and the nnn hopping strength $t'$ as well as the in-plane Zeeman field are tunable parameters.

### A. System with only Dresselhaus SO interaction

We start our investigations with a perfect $24 \times 40$ rectangular system when the Dresselhaus SO interaction is solely introduced, and Fig. 1 displays the contour plots of different topological defect states with increasing applied magnetic flux $\Phi$. The rows (a) and (b) in Fig. 1 give the amplitude $|\Delta_s|$ and phase $\phi_s$ for the extended $s$-wave order. Similarly, rows (c) and (d) show the corresponding spatial profiles for the $d$-wave order. The row (e) demonstrates the relative phase $\phi_{sd}$ between the mixed $s$- and $d$-wave components. One can clearly see that $d$-wave and extended $s$-wave condensates can coexist with comparable strength in our finite-size case. At zero out-of-plane flux (the leftmost column), the dominant $d$-wave and subdominant $s$-wave order parameters both take on a constant magnitude inside the sample. Meanwhile, the relative phase $\phi_{sd} = \cos(\phi_s - \phi_d)$ between them is close to zero, forming the favored $s + id$-wave state with broken time-reversal symmetry.
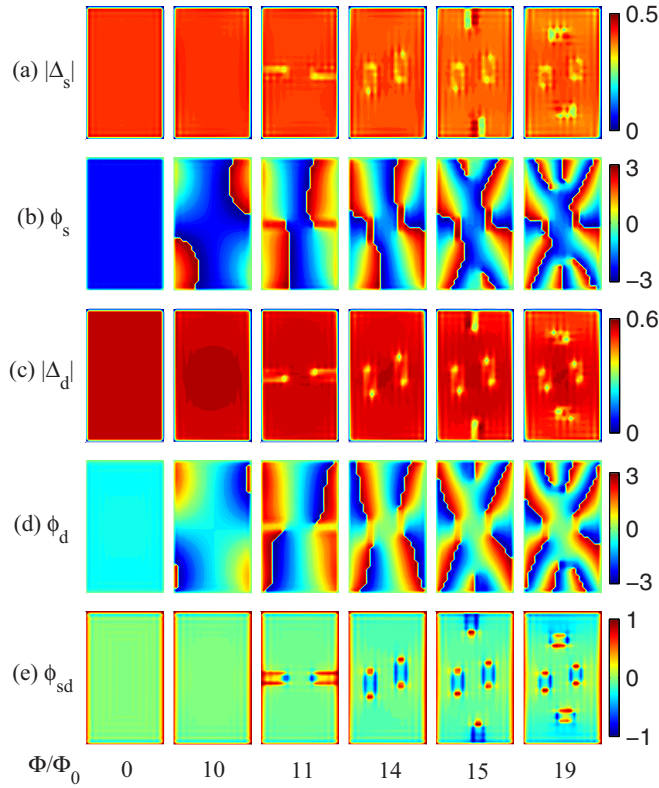
FIG. 1. Spatial profiles of topological defect states at different applied magnetic flux $\Phi$ in a mesoscopic rectangle with $N_x \times N_y = 24 \times 40$ when $V_{Rso} = 0$ and $t' = 0$. Rows (a)–(b): the amplitude $|\Delta_s|$ and phase $\phi_s$ for the extended $s$-wave order; rows (c)–(d): the amplitude $|\Delta_d|$ and phase $\phi_d$ for the $d$-wave order; row (e): the relative phase $\phi_{sd} = \cos(\phi_s - \phi_d)$ between the $s$- and $d$-wave components. The calculation is performed for $V = 5$, $\mu = -2$, and $V_{Dso} = 0.3$ at zero temperature.

When a small finite flux turns on, the ground state of our system with pure Dresselhaus SO coupling is still the vortex-free state, analogous to the Meissner state in conventional $s$-wave superconductors. As shown in the second column of Fig. 1 when $\Phi/\Phi_0 = 10$, there is no flux trapped in the rectangle and only the regions near long sides of outer edges are influenced. With increasing flux, two one-component vortices in both $s$- and $d$-wave condensates can simultaneously enter the sample from the middle of two long sides along the horizontal direction at some critical flux value. Then, the unclosed domain-wall states can stabilize near the long boundaries. As an illustrative example, the third column of Fig. 1 depicts the general picture of this state when $\Phi = 11\Phi_0$. Two vortices penetrate the sample's edge and are localized near the rectangular center in $\Delta_s$ and $\Delta_d$ each, which can be clearly revealed in the phase plots for these two coupled condensates. As shown in the $\phi_s$ and $\phi_d$ panels, phases near $-\pi$ are given by blue regions and phases near $\pi$ by red regions. When encircling the region near the vortex core counterclockwise, the phase changes $1 \times 2\pi$, which means the vorticity $L = 1$. Particularly, the singly quantized vortex state with two overlapped one-component vortices does not take place, although the vortex cores in $\Delta_s$ and $\Delta_d$ are very close. Instead, the domain-wall bound state with an unclosed vortex
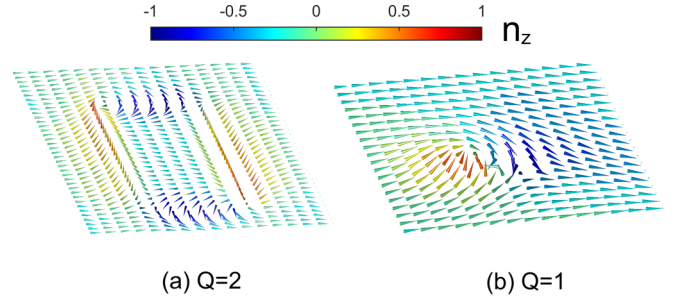


FIG. 2. The pseudospin texture $\mathbf{n}(x, y)$ of the double-quanta skyrmion with the topological charge $Q = 2$ shown in the fourth column of Fig. 1(a) and the single-quanta one with $Q = 1$ shown in the second column of Fig. 3(b). The color indicates the amplitude of the $z$ component of the pseudospin field $\mathbf{n}(x, y)$.

chain occurs, indicating the possible presence of multibody intervortex interactions in superconductors with competing order parameters [53]. Note that additional vortices are failed to penetrate the long edges of the rectangle due to the presence of energy barriers, while the attraction of one-component vortices towards the mesoscopic edges provides stability to the continuous chain structure. As depicted in the $\phi_{sd}$ profile, half of total four individual vortices align their cores to give rise to one of the two opposite unclosed chains, and $\phi_{sd}$ alternates two times between negative and positive values on each domain wall.

If we keep increasing the applied external field, more flux will nucleate inside the mesoscopic rectangle. Similar to the vortex evolution discussed above, one can find that two one-component vortices in $\Delta_s$ and $\Delta_d$ each enter the sample from the middle of the left and right long sides and a striking type of topological defect states can stabilize. As clearly displayed in the fourth column of Fig. 1 for an enlarged $\Phi/\Phi_0 = 14$, four one-component vortices in $s$- and $d$-wave orders do not coincide in space near the left and right edges. Thus, they can combine into a topological structure that exhibits skyrmionic character. Correspondingly in the profile of $\phi_{sd}$, a rectangular-loop-like phase domain wall, where four shift nodes correspond to the location of four one-component vortices, can be seen near both long sides, i.e., a coreless vortical structure carrying two flux quanta is formed. The skyrmionic feature of such a coreless vortex can be clearly revealed by the corresponding pseudospin texture $\mathbf{n}$, as plotted in the left panel of Fig. 2. It is seen that the $n_z$ projection of the pseudospin rotates along the domain wall by $4\pi$, resulting in the net topological charge $Q = 2$. Notice that the spatial structure of the enclosed vortex chain is modulated by the noncircular shape in our mesoscopic system. In this situation, two enclosed vortex chains are elongated vertically and compressed horizontally as a result of the aspect-ratio effect. Moreover, such two double-quanta skyrmions tend to stabilize along one of the diagonal directions. We may attribute this to the reduction of the symmetry of Fermi surfaces from $C_4$ to $C_2$ once a finite Dresselhaus SO coupling is included into the system [46].

With further enlarging the external magnetic flux, the $L_{s(d)}$ vorticities increase with flux, and more complex topological patterns can be obtained. Two representative examples are
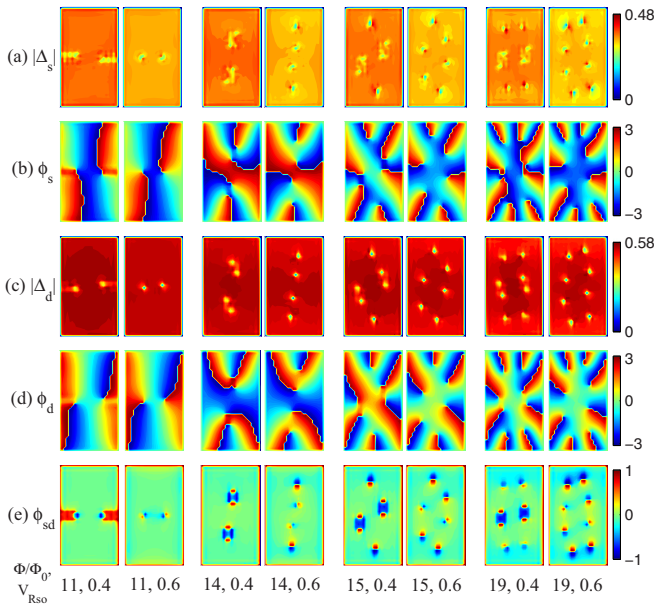
FIG. 3. Spatial profiles of topological defect states at different flux $\Phi/\Phi_0$ for finite values of $V_{Rso}$ in a mesoscopic $24 \times 40$ rectangle. Displayed quantities are the same as in Fig. 1. The calculation is performed for $V = 5$, $\mu = -2$, and $V_{Dso} = 0.3$ at zero temperature.



FIG. 4. (a) The averaged order parameters $|\Delta_s|$ and $|\Delta_d|$ for the extended $s$-wave and $d$-wave pairing symmetries as a function of $V_{Rso}$ at $\Phi/\Phi_0 = 11$ in the mesoscopic $24 \times 40$ rectangle. (b) The averaged $|\Delta_s|$ and $|\Delta_d|$ as a function of $t'$ for $V_{Rso} = 0.4$ at $\Phi/\Phi_0 = 11$ in the mesoscopic $24 \times 40$ rectangle. The calculation is performed for $V = 5$, $\mu = -2$, and $V_{Dso} = 0.3$ at zero temperature.

given in two rightmost columns of Fig. 1. One can see that a hybrid topological defect state containing two enclosed skyrmions inside the sample and two unclosed domain-wall structures near the short sides shows up when $\Phi = 15\Phi_0$. By contrast, a multiskyrmionic configuration with four rectangular-loop-like skyrmions surrounded the sample center can emerge at a higher $\Phi = 19\Phi_0$. It is noted that the vortex penetration through the long sides is no longer found due to the influence of stronger vortex-vortex repulsion along the horizontal direction. In these cases, one-component vortices can enter the sample through the short sides two by two for each of orders. Simultaneously, the closed domain walls of two newly formed skyrmions near the short sides tend to be elongated along the horizontal direction. Such multiple features can be easily distinguished according to their signatures in the $\phi_{sd}$ plots.

### B. System with combined Rashba and Dresselhaus SO couplings

In this section, we would like to investigate characteristic vortex configurations when the admixed Rashba SO interaction is involved in the mesoscopic rectangular system. It is known that the ratio between Rashba and Dresselhaus SO couplings greatly influences the spin textures and topological edge state [45–47]. Figure 3 displays the spatial profiles of topological defect states induced by finite $V_{Rso}$ at different flux values. As compared to the case with solely Dresselhaus SO interaction in the third column of Fig. 1, the unclosed domain-wall state can still be observed for a weak $V_{Rso}$ when $\Phi/\Phi_0 = 11$ (see the first column when $V_{Rso} = 0.4$). However, the positions of two one-component vortices interconnecting to form the unclosed vortex chain tend to be modified by the relative Rashba magnitude. For a sufficiently strong $V_{Rso}$, the superconducting phase transitions between different vortex
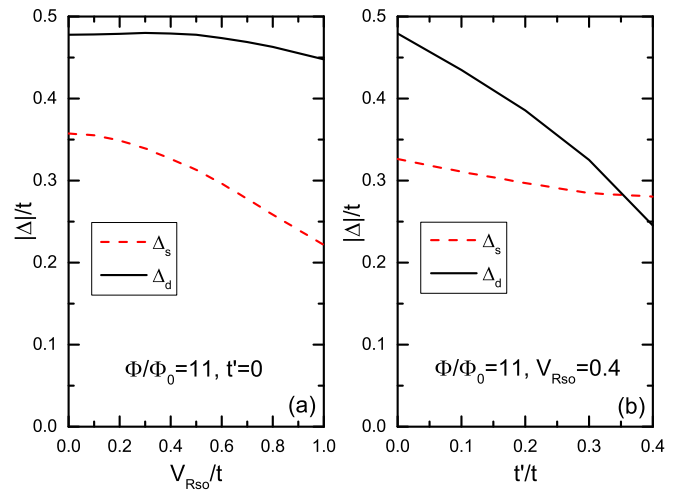
states are expected to take place in the Rashba-dominated regime. In Fig. 4(a), we plot the corresponding averaged order parameters over all lattice sites as a function of $V_{Rso}$ when $\Phi/\Phi_0 = 11$. One can see that there generally exists a destructive effect of the Rashba SO coupling on the dominant $d$-wave order. By contrast, the subdominant $s$-wave order is highly suppressed with increasing $V_{Rso}$. As a consequence, the vortices per component favor to move toward the sample's center. As depicted in the second column of Fig. 3 when $V_{Rso} = 0.6$, two adjacent one-component vortices combine to form a new coreless vortex state in both left and right halves of the rectangle, i.e., the single-quanta skyrmionic pattern with split cores between the component condensates may arise in the present system with mixed-pairing symmetries. Such a skyrmionic topological defect with $Q = 1$ can be demonstrated from Fig. 2(b) where the $z$ component of the pseudospin flips two times when moving along the domain wall. Notice that the single-quanta skyrmion manifests as twofold symmetry, similar to the skyrmionic mode with unit topological charge as a lowest-energy topological excitation in two-component nematic superconductors [41,42]. In addition, the singular vortex with a pointlike core, which always exhibits a cloverleaf pattern in the relative phase profile [38], is hard to reach here due to present disbalance between the coexisted orders.

Next we present the topological defect states exposed to larger perpendicular flux when the effects of Rashba SO interaction is included. Interestingly in the third column of Fig. 3 when $\Phi/\Phi_0 = 14$, one can find that the multiskyrmion states containing two $Q = 2$ skyrmions can still be found for a weak $V_{Rso} = 0.4$, while the skyrmions tend to move and stabilize in a line along the long side of the rectangle in comparison to the case without Rashba SO interaction in Fig. 1. Particularly, the $Q = 2$ skyrmionic configuration becomes unstable and splits up into two parts for further enlarged $V_{Rso}$, leading to the emergence of a novel multiskyrmion state with four
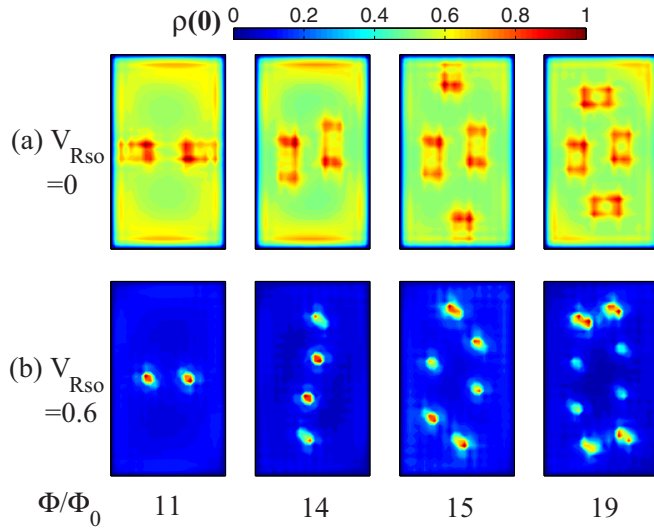
FIG. 5. Spatial profiles of the zero-energy local density of states $\rho(0)$ for topological defect states at different flux when $V_{Rso} = 0$ in Fig. 1 [row (a)] and when $V_{Rso} = 0.6$ in Fig. 3 [row (b)] in a mesoscopic $24 \times 40$ rectangle. The calculation is performed for $V = 5$, $\mu = -2$, $t' = 0$, and $V_{Dso} = 0.3$ at zero temperature.



FIG. 6. Spatial profiles of topological defect states for different values of $t'$ at the magnetic flux $\Phi/\Phi_0 = 11$ [panels (I)] and 15 [panels (II)] in contrast to the corresponding $t' = 0$ case in Fig. 3. Panels (III) depict the evolution process of skyrmions with increasing the strength $\mathbf{h}_y$ of an in-plane Zeeman field applied along the $y$ direction. Displayed quantities are the same as in Fig. 1. The calculation is performed for $V = 5$, $\mu = -2$, and $V_{Dso} = 0.3$ at zero temperature.

$Q = 1$ skyrmions, as clearly revealed in the fourth column of Fig. 3. Similarly, the four right columns in Fig. 3 show the influences of $V_{Rso}$ on the phase transitions between topological defects in our rectangular system when $\Phi/\Phi_0 = 15$ and 19. Generally, as compared to the corresponding pure Dresselhaus SO-coupling cases at the same flux values in Fig. 1, we can conclude that the unclosed domain-wall states near the boundaries will enter the sample and the $Q = 2$ skyrmions cannot remain and will split with increasing $V_{Rso}$, accompanied with the occurrence of topological defect structures with multiple $Q = 1$ skyrmions. Notably, our asymmetric rectangular geometry will favor different arrangements of $Q = 1$ skyrmion lattices. We can find that the skyrmion lattice structure tries to evolve into a triangular shape in the order-parameter space (see the sixth column of Fig. 3 when $\Phi/\Phi_0 = 15$ and $V_{Rso} = 0.6$). By contrast, when two extra $Q = 1$ skyrmions are generated inside the sample (the rightmost column when $\Phi/\Phi_0 = 19$ and $V_{Rso} = 0.6$), the triangular lattice configuration is somewhat deformed in such a case because of the influences of vortex-vortex repulsion and geometric effect.

Moreover, the spatial variations of LDOS at zero energy corresponding to the presented topological defects with and without Rashba SO coupling are depicted in Fig. 5. Clearly for the case of $V_{Rso} = 0$ [the top row (a)], the zero-bias peaks mainly appear at the unclosed or closed domain walls as a result of the existence of domain-wall bound states corresponding to the coreless vortex states in Fig. 1. In the bottom row (b) of Fig. 5, we also calculate the distributions of zero-energy LDOS for $Q = 1$ skyrmions at different flux cases in Fig. 3 when $V_{Dso} = 0.6$. Apparently, the elongated zero-bias peaks in the LDOS profile reveal the occurrence of unusual vortex bound states, in agreement with images of vortices observed in nematic superconductors [54]. Particularly, unique twin-peak structures can be found in the right
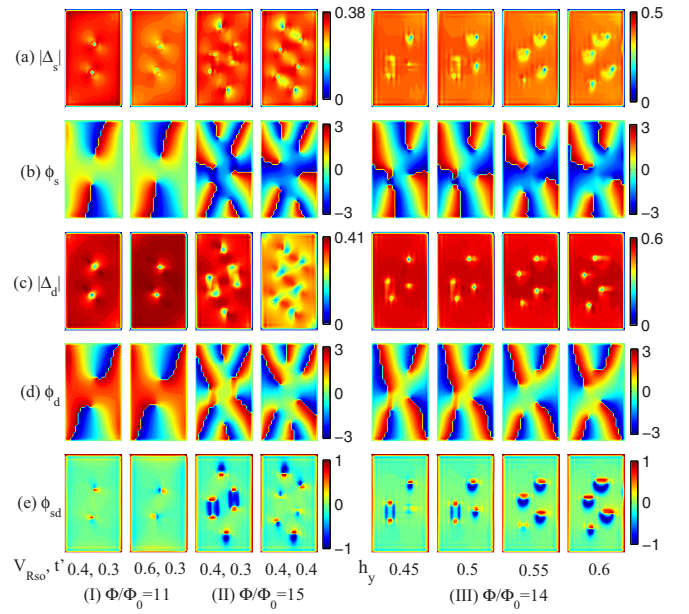
panel when $\Phi/\Phi_0 = 19$ due to the existence of two separated one-component vortices for a single-quanta skyrmion. Notice that such two adjacent zero-bias peaks for a $Q = 1$ skyrmion tend to merge together around the sample's center as a result of the finite-size effect, presenting a similar feature as the case of a singly quantized vortex.

## C. Effects of nnn hopping and in-plane Zeeman field on the vortical configurations

Apart from the Rashba SO coupling, we also consider the effects of nnn hopping and in-plane Zeeman field on the vortex matter in our mixed-pairing system. Notably, the finite nnn hopping in the Hubbard model is an important electronic parameter characterizing superconducting materials [55]. Hence, we first introduce the nnn hopping in the effective model Hamiltonian and examine the evolution of topological defect states by tuning the magnitude $t'$ of the nnn hopping. As seen in the panels (I) of Fig. 6 when $\Phi/\Phi_0 = 11$, the spatial order-parameter distributions for the cases of $V_{Rso} = 0.4$ and 0.6 are given when $t' = 0.3$. Comparing to the case of $t' = 0$ in the first column of Fig. 3 at the same values of $\Phi$ and $V_{Rso}$, the unclosed domain-wall state becomes unstable near the rectangular long sides for a finite $t'$ resulting from the modification of relative strengths of competing pairing symmetries. In Fig. 4(b), we show the corresponding evolution of averaged order parameters as a function of $t'$ when $V_{Rso} = 0.4$. It is obvious that the amplitude of dominant $d$-wave component is highly reduced with increasing $t'$ compared to the $s$-wave one, leading to a clear change of the dominant order from $d$-wave to $s$-wave pairing. As a result,

the unclosed domain-wall chains disappear and two enclosed coreless chains carrying unit topological charge each favor to occur, as depicted in the first column of Fig. 6. Simultaneously, the vortices in both *s*- and *d*-wave components will rotate nearly $\pi/2$ when $t'$ is varied, and two formed $Q = 1$ skyrmions stabilize almost along the vertical direction as a result of the confinement of the rectangular shape. Likewise, the positions of single-quanta skyrmions generated in the situation of $t' = 0$ is also sensitive to the effect of nnn hopping. As displayed in the second column of Fig. 6 when $V_{\mathrm{Rso}} = 0.6$, the vortex configuration can be rearranged for a finite $t' = 0.3$ in contrast to the $t' = 0$ case shown in the second column of Fig. 3, and two $Q = 1$ skyrmions tend to be situated along the direction in parallel with the long edge of the sample analogous to the stable mode shown in the first column.

Moreover, the superconducting phase transition between the $Q = 2$ and $Q = 1$ skyrmions can also take place when a finite nnn hopping is introduced. The panels (II) of Fig. 6 give a representative sample for such an evolution process when $\Phi/\Phi_0 = 15$ and $V_{\mathrm{Rso}} = 0.4$. As compared to the case without $t'$ in the fifth column of Fig. 3, the topological defect structures with hybrid $Q = 2$ and $Q = 1$ skyrmions can still stabilize for a small value of $t'$, while the domain-wall structure of $Q = 2$ skyrmions is deformed in the vertical direction (see the third column when $t' = 0.3$). If $t'$ is further enlarged, the strength of the *d*-wave order is highly suppressed, and the core sites of vortices in this condensate will be effectively tuned (see the fourth column when $t' = 0.4$). Consequently, the $Q = 2$ skyrmions around the rectangular center both split, and the multiple $Q = 1$ skyrmionic mode can be realized in the order-parameter space.

In the next step, let us turn our attention to the effect of a Zeeman field lying in the two-dimensional plane and examine the peculiar phase transitions driven by the in-plane Zeeman potential. It is noted that the in-plane Zeeman field can cause a nonmonotonic energy shift for the bulk energy spectrum and also suppress the superconducting gap size [49]. Bulk and boundary topological phase transitions can be induced, relying on the direction and strength of applied in-plane Zeeman field [56]. According to above analysis, one $Q = 2$ skyrmion favors to stretch along the long side and split the one-component vortex chain to form two $Q = 1$ skyrmions in our present rectangular system. Thus, we mainly examine the effect of Zeeman field applied in the *y* direction (i.e., parallel to the long side of the rectangle) here. As a representative instance, the panels (III) in Fig. 6 demonstrate the evolution of spatial distributions of the order parameter at $\Phi = 14\Phi_0$ as a result of an increasing in-plane Zeeman field when $V_{\mathrm{Rso}} = 0$ and $t' = 0$. Indeed, for the multiskyrmionic state with two $Q = 2$ skyrmions shown in the fourth column of Fig. 1, a finite $\mathbf{h}_y$ can lead to the breaking of two enclosed domain walls one by one along the vertical direction according to the signatures in the phase difference $\phi_{sd}$ plots. Simultaneously, two neighboring one-component vortices interconnect to form one single-quanta skyrmion. It is noted that the skyrmion size depends on the applied Zeeman field and can expand along the horizontal direction by further increasing the field strength. Consequently, four enclosed coreless chains with the obvious looplike feature show up for an appropriate $\mathbf{h}_y$.
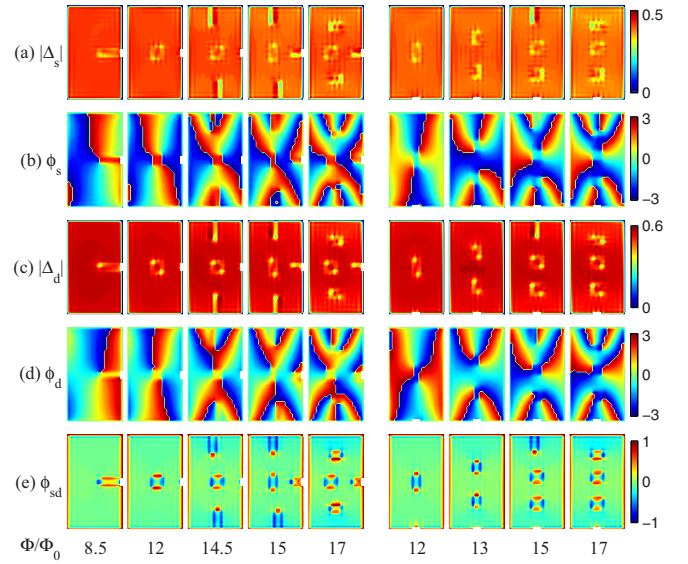


FIG. 7. Spatial profiles of topological defect states at different applied flux $\Phi$ in a mesoscopic $24 \times 40$ rectangle with a surface indentation defect in the middle of the long side (five columns on the left) and with one in the middle of the short side (four columns on the right) when $V_{\mathrm{Rso}} = 0$ and $t' = 0$. Displayed quantities are the same as in Fig. 1. The calculation is performed for $V = 5$, $\mu = -2$, and $V_{\mathrm{Dso}} = 0.3$ at zero temperature.

## IV. TOPOLOGICAL DEFECT STATES IN SUPERCONDUCTING RECTANGLES WITH SURFACE DEFECTS

In the above sections, we concentrated on the vortical configurations in a perfect smooth rectangle. It is noted that a superconductor with surface roughness is inevitable in experiments and one should deal theoretically with defects at the surface. A surface indentation defect can act as the nucleation center for vortex entry, which decrease the surface barrier [50]. Therefore, we turn to study the effect of surface defects on vortex penetration in this section and only consider a small indentation defect with fixed length $l = 3$ and depth $d = 1$ placed at the middle of the long or the short side of the rectangle.

Figure 7 gives the evolution of vortex states at different applied flux $\Phi$ in a mesoscopic $24 \times 40$ rectangle with the surface indentation defect in the middle of the long side (four columns on the left) and with one in the middle of the short side (four columns on the right) when $V_{\mathrm{Rso}} = 0$ and $t' = 0$. For the perfect rectangle without surface defects in Fig. 1, two vortices for each component enter the sample opposite to each other from the middle of the long sides at the first penetration field. By contrast, a defect with size $l \times d = 3 \times 1$ in the middle of the right long side can highly change the first vortex entry and also the vorticity $L$. As shown in the first column of Fig. 7, the one-component vortex can penetrate the sample at a reduced flux $\Phi/\Phi_0 = 8.5$ because the surface defect is introduced at the entering position of the vortex. Meanwhile, only one vortex per component enters from the defect position when the vortex-free state becomes unstable. Thus, just one unclosed domain wall appears and can stabilize near the right long edge of the rectangle at weak flux as a result

of the suppression of narrow edges, as seen in the $\phi_{sd}$ plot. With increasing flux, the second one-component vortex still enters through the defect and combines with the first nucleated one, leading to one $Q = 2$ skyrmion inside the sample (see the second column in Fig. 7). Due to the presence of the skyrmion in the center of the rectangle, the new entering vortex through the defect for further enlarged flux is repelled by this adjacent skyrmion. Simultaneously, two new preferable entry positions for vortices are created along the two short edges. As a consequence, one can observe two unclosed domain-wall structure developed first near the short boundaries and then the third one from the defect site in the third to fourth columns of Fig. 7. If we keep increasing the field, because of the stronger repulsion between the vortices along the horizontal direction, additional one-component vortices are easier to enter from the short edges in both $s$ and $d$ condensates, and then two $Q = 2$ skyrmions are newly formed inside the rectangle (see the fifth column in Fig. 7).

In contrast, if the same surface indentation defect is added in the middle of the bottom short edge, we checked that the first penetration field is nearly the same as the one for the perfect rectangle in Fig. 1. However, the surface defect can act as an easier position for first vortex penetration in this situation. One vortex per component enters the sample through the middle of the short side where the defect is located, while the domain-wall state containing one unclosed vortex chain is hard to stabilize now due to the weak confinement effect along the vertical direction parallel to the long edge. Thus, the second one-component vortex enters through the defect at the next penetration field until a $Q = 2$ skyrmionic state stabilizes at the rectangle's center, as clearly seen in the sixth column of Fig. 7 when $\Phi/\Phi_0 = 12$. Similarly, the one-component vortices enter one by one through the defect site and another $Q = 2$ skyrmion can emerge at higher fields (see the seventh column). Interestingly, for further increased flux, the top short edge can act effectively as a new nucleation center for vortex entry instead of the surface defect and the long edges due to the rectangle's aspect-ratio effect as well as the interplay between the vortex-vortex repulsion. As displayed in the two rightmost columns in Fig. 7, one can find the formation of an unclosed domain wall and then a $Q = 2$ skyrmion near the upper short edge with increasing field.

Next, we investigate the influence of the admixed Rashba SO interaction on the skyrmion structure, and the corresponding results are given in Fig. 8. It is already known that the relative strength of competing $s$ and $d$ condensates is controllable when the Rashba SO coupling is included in the perfect rectangular system in above section. However, only multiskyrmionic patterns with even number of single-quanta coreless skyrmions can be found in such a perfect system. Notice that, once the surface defect is introduced into the sample, topological defect states containing odd number of unclosed domain walls have been predicted to generate in the imperfect system (see Fig. 7). Thus, similar to the evolution process described in the perfect case, the location and number of the $Q = 1$ skyrmions can be effectively tuned in the presence of combined effect of Rashba and Dresselhaus SO interactions and several novel $Q = 1$ skyrmionic states should be obtained. Clearly in Fig. 8 where the spatial profiles of topological defects are depicted for the rectangle with a surface indentation
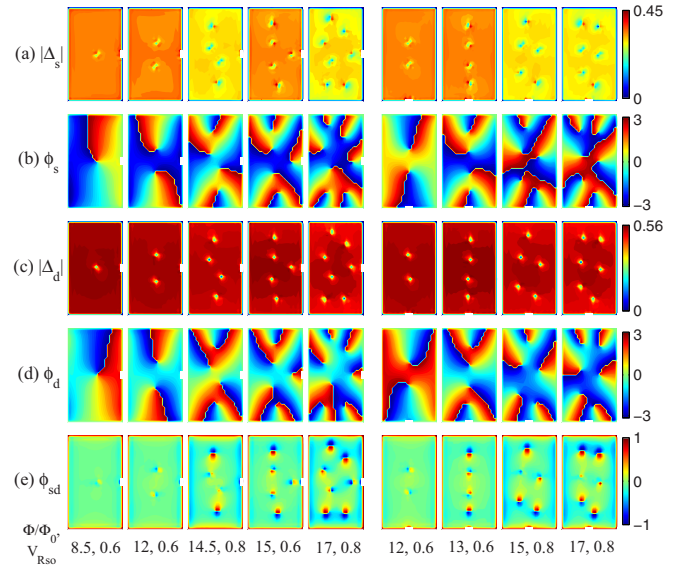


FIG. 8. Spatial profiles of topological defect states at different applied flux $\Phi$ in a mesoscopic $24 \times 40$ rectangle with a surface indentation defect in the middle of the long side (five columns on the left) and with one in the middle of the short side (four columns on the right) when a finite $V_{Rso}$ is introduced. Displayed quantities are the same as in Fig. 7. The calculation is performed for $V = 5$, $\mu = -2$, $t' = 0$, and $V_{Dso} = 0.3$ at zero temperature.

defect in the middle of the long side (five columns on the left) or with one in the middle of the short side (four columns on the right), the unclosed domain wall and the $Q = 2$ skyrmion can both transform into the $Q = 1$ skyrmion beyond a critical $V_{Rso}$ for different flux values, accompanied with the emergence of peculiar single-skyrmionic and multiskyrmionic states consisting of odd number of $Q = 1$ skyrmions. Meanwhile, the spatial profiles of $Q = 1$ skyrmions are modulated by the rectangular shape and the surface defect as well as the vortex-vortex interaction, leading to rich stable configurations with skyrmionic character.

Finally, we discuss how the in-plane Zeeman field induces a singular $Q = 1$ skyrmion and affects its structure in a rectangle with a surface indentation defect in the middle of the long edge. The left panels (I) in Fig. 9 present the corresponding evolution from the unclosed domain-wall state to the single-skyrmion state for in-plane Zeeman fields applied along the $x$ and $y$ directions in the sample with pure Dresselhaus SO interaction when $\Phi/\Phi_0 = 8.5$. The contribution from the Zeeman potential will cause unusual behaviors in the present case with only one unclosed domain-wall structure because of the asymmetric effect. Clearly in the two leftmost columns, the attraction of the one-component vortex towards the defect is destroyed across a critical $\mathbf{h}_x$. Consequently as expected, a singular $Q = 1$ skyrmionic state, which carries two one-component vortices aligning along the $y$ direction arises inside the sample. Particularly, if we rotate the direction of the Zeeman field by $\pi/2$, the unclosed domain wall can also be tuned by a finite $\mathbf{h}_y$ (see the third column). One can observe the resulting $Q = 1$ skyrmion due to the absence of vortex-vortex repulsion along the short side (the fourth column). In addition, for the formed $Q = 1$ skyrmion shown
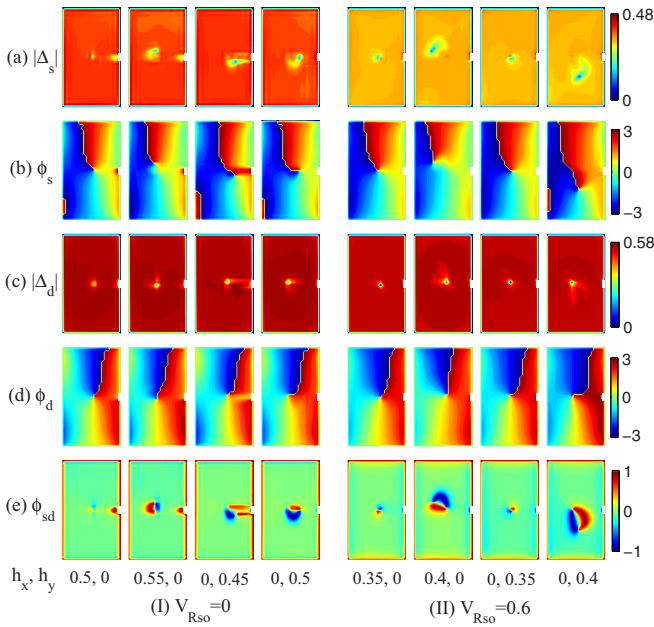
FIG. 9. Spatial profiles of topological defect states at the magnetic flux $\Phi/\Phi_0 = 8.5$ for different $\mathbf{h}_x$ and $\mathbf{h}_y$ in a mesoscopic $24 \times 40$ rectangle with a surface indentation defect in the middle of the long edge when $V_{Rso} = 0$ [left panels (I)] and $V_{Rso} = 0.6$ [right panels (II)]. Displayed quantities are the same as in Fig. 7. The calculation is performed for $V = 5$, $\mu = -2$, $t' = 0$, and $V_{Dso} = 0.3$ at zero temperature.

in the first column of Fig. 8 when $V_{Rso} = 0.6$, a finite in-plane Zeeman field can highly influence the distance between one-component vortex cores. As displayed in panels (II) of Fig. 9, the two one-component vortices trapped in an enclosed domain wall have more separated cores in the horizontal direction with increasing $\mathbf{h}_x$. In comparison, an enlarged $\mathbf{h}_y$ can elongate the closed vortex chains along the vertical direction due to the anisotropic effect of in-plane Zeeman fields. As a result, the skyrmionic topological feature that is characterized by a coreless vortex structure in the $\phi_{sd}$ plots can be readily found.

## V. CONCLUSIONS

In conclusion, we have systematically investigated the possible topological defect states and the associated phase transitions in a mesoscopic superconducting rectangular system with mixed $d$-wave and extended $s$-wave condensates in the presence of SO interactions. We performed numerically self-consistent calculations using the spin-generalized BdG equations. By suitable choice of model parameters, the $s + id$ superconducting phase with broken time-reversal symmetry can be obtained in the present system. For the case with only the Dresselhaus SO interaction, one can observe the unclosed domain walls near outer boundaries and double-quanta coreless skyrmionic patterns inside the sample under applied out-of-plane magnetic flux due to present disbalance between two competing orders. Interestingly, when the admixed Rashba SO coupling is involved, the single-quanta coreless skyrmion with unit topological charge $Q = 1$ favors to form in our rectangular system. Meanwhile, the relative strength

of competing pairing symmetries can be effectively tuned by the strengths of Rashba SO coupling and nnn hopping, giving rise to several peculiar multiple and hybrid topological defect structures containing even number of $Q = 1$ skyrmions. Moreover, the influence of in-plane Zeeman field on the phase transitions of order-parameter modulations was revealed. An appropriate in-plane Zeeman potential with a certain applied direction can drive the splitting of unclosed and enclosed domain-wall structures, accompanied with the emergence of obvious single-quanta skyrmionic feature. Finally, the effect of surface defects on the position and number of topological defects was studied, together with the influences of Rashba SO coupling and in-plane Zeeman field. By introducing a defect in the middle of the short or the long side of the rectangle, the single-skyrmionic and multiskyrmionic states hosting odd number of $Q = 1$ skyrmions can also be produced in our mixed-pairing system.

Our theoretical results clearly demonstrate that several distinct classes of vortical configurations, especially the single-quanta skyrmionic state, can arise stably in the rectangular system with coupled condensates in the presence of the SO interaction. With the development of experimental techniques, nanostructured superconducting samples with different shapes are possible to be fabricated. Also, SO interactions related to the inversion asymmetry may be created at surfaces and interfaces of superconductors, and the Zeeman field can be generated by exchange interaction in a quantum material. Therefore, our investigations might provide an experimental setup to detect and manipulate topological defect states in multicomponent superconducting systems. Moreover, our calculations can be useful for some relevant systems, such as the copper-oxide and iron-based superconductors with $s + id$ superconductivity [57–60]. In addition, one can experimentally consider placing surface defects at different edges of the sample according to our results, in order to fine tune the path of vortex entry and superconducting phase transition. A quantized superconducting vortex can be used as an information bit, which is utilized for creation of high-density digital cryoelectronics [61]. Particularly, the half-quantum vortices are known to host Majorana zero modes, with possible implementation of quantum computing. The one-component vortices are spatially separated in the skyrmionic configuration and each of them carries half vorticity of a full vortex, which may be rather easily stabilized in mesoscopic superconducting samples. We expect that our theoretical predictions will be verified experimentally and may provide useful guidance for futuristic applications in superconducting electronics.

Finally, we remark that the mixed-pairing case consisting of $d_{x^2-y^2}$-wave and extended $s$-wave symmetries is mainly considered in our BdG simulations. In contrast to the time-reversal-symmetry-broken $s \pm id$-wave state induced in the present rectangular lattice, new effective pairings may be stabilized within the same type of interaction for other finite lattice systems. For instance, a highly unconventional superconducting state with a spin-singlet $d_{x^2-y^2} \pm id_{xy}$-wave, i.e., the chiral $d$-wave symmetry, can emerge in graphene, which is intimately linked to the hexagonal crystal lattice and edge modes [62]. Since the chiral superconductivity is characterized by the breaking of time-reversal symmetry, rich

phenomena related to the tunable vortical and skyrmionic states may take place in such multicomponent superconducting systems [63].

[1] R. Winkler, S. J. Papadakis, E. P. De Poortere, and M. Shayegan, *Advances in Solid State Physics: Spin-Orbit Coupling in Two-Dimensional Electron and Hole Systems*, Vol. 41 (Springer, 2003).

[2] V. Galitski and I. B. Spielman, Spin-orbit coupling in quantum gases, Nature (London) **494**, 49 (2013).

[3] K. Zakeri, D. Rau, J. Jandke, F. Yang, W. Wulfhekel, and C. Berthod, Direct probing of a large spin-orbit coupling in the FeSe superconducting monolayer on STO, ACS Nano **17**, 9575 (2023).

[4] E. I. Rashba, Symmetry of energy bands in crystals of wurtzite-type: I. Symmetry of bands disregarding spin-orbit interaction, Sov. Phys. Solid State **1**, 368 (1959).

[5] G. Dresselhaus, Spin-orbit coupling effects in zinc blende structures, Phys. Rev. **100**, 580 (1955).

[6] C. O. Dias, H. O. Frota, and A. Ghosh, Superconducting and DDW states of high-$T_c$ cuprates with Rashba and Dresselhaus spin–orbit couplings, Phys. Status Solidi B **253**, 1824 (2016).

[7] L. P. Gor'kov and E. I. Rashba, Superconducting 2D system with lifted spin degeneracy: Mixed singlet-triplet state, Phys. Rev. Lett. **87**, 037004 (2001).

[8] M. H. Fischer, M. Sigrist, and D. F. Agterberg, Superconductivity without inversion and time-reversal symmetries, Phys. Rev. Lett. **121**, 157003 (2018).

[9] X.-L. Qi and S.-C. Zhang, Topological insulators and superconductors, Rev. Mod. Phys. **83**, 1057 (2011).

[10] J. Alicea, New directions in the pursuit of Majorana fermions in solid state systems, Rep. Prog. Phys. **75**, 076501 (2012).

[11] G.-Q. Zha, L. Covaci, F. M. Peeters, and S.-P. Zhou, Majorana zero-energy modes and spin current evolution in mesoscopic superconducting loop systems with spin-orbit interaction, Phys. Rev. B **92**, 094516 (2015).

[12] B. Lian, X.-Q. Sun, A. Vaezi, X.-L. Qi, and S.-C. Zhang, Topological quantum computation based on chiral Majorana fermions, Proc. Natl. Acad. Sci. USA **115**, 10938 (2018).

[13] Y. Volpez, D. Loss, and J. Klinovaja, Second-order topological superconductivity in $\pi$-junction Rashba layers, Phys. Rev. Lett. **122**, 126402 (2019).

[14] X. Zhu, Second-order topological superconductors with mixed pairing, Phys. Rev. Lett. **122**, 236401 (2019).

[15] Z. Yan, Higher-order topological odd-parity superconductors, Phys. Rev. Lett. **123**, 177001 (2019).

[16] M. Kheirkhah, Z. Yan, Y. Nagai, and F. Marsiglio, First-and second-order topological superconductivity and temperature-driven topological phase transitions in the extended hubbard model with spin-orbit coupling, Phys. Rev. Lett. **125**, 017001 (2020).

[17] A. Y. Kitaev, Unpaired Majorana fermions in quantum wires, Phys. Usp. **44**, 131 (2001).

[18] L. Fu and C. L. Kane, Superconducting proximity effect and Majorana fermions at the surface of a topological insulator, Phys. Rev. Lett. **100**, 096407 (2008).

[19] C. Nayak, S. H. Simon, A. Stern, M. Freedman, and S. D. Sarma, Non-Abelian anyons and topological quantum computation, Rev. Mod. Phys. **80**, 1083 (2008).

[20] J. D. S. Bommer, H. Zhang, O. Gul, B. Nijholt, M. Wimmer, F. N. Rybakov, J. Garaud, D. Rodic, E. Babaev, M. Troyer, D. Car, S. R. Plissard, E. P. A. M. Bakkers, K. Watanabe, T. Taniguchi, and L. P. Kouwenhoven, Spin-orbit protection of induced superconductivity in Majorana nanowires, Phys. Rev. Lett. **122**, 187702 (2019).

[21] C. C. Tsuei, J. R. Kirtley, C. C. Chi, L. S. Y. Jahnes, A. Gupta, T. Shaw, J. Z. Sun, and M. B. Ketchen, Pairing symmetry and flux quantization in a tricrystal superconducting ring of YBa$_2$Cu$_3$O$_{7-\delta}$, Phys. Rev. Lett. **73**, 593 (1994).

[22] E. Babaev and M. Speight, Semi-Meissner state and neither type-I nor type-II superconductivity in multicomponent superconductors, Phys. Rev. B **72**, 180502(R) (2005).

[23] S.-Z. Lin and X. Hu, Vortex states and the phase diagram of a multiple-component Ginzburg-Landau theory with competing repulsive and attractive vortex interactions, Phys. Rev. B **84**, 214505 (2011).

[24] M. Sigrist, T. M. Rice, and K. Ueda, Low-field magnetic response of complex superconductors, Phys. Rev. Lett. **63**, 1727 (1989).

[25] M. Matsumoto and M. Sigrist, Quasiparticle states near the surface and the domain wall in a $p_x \pm ip_y$-wave superconductor, J. Phys. Soc. Jpn. **68**, 994 (1999).

[26] V. F. Becerra and M. V. Milosevic, Multichiral ground states in mesoscopic $p$-wave superconductors, Phys. Rev. B **94**, 184517 (2016).

[27] L.-F. Zhang, L. Covaci, and M. V. Milosevic, Topological phase transitions in small mesoscopic chiral $p$-wave superconductors, Phys. Rev. B **96**, 224512 (2017).

[28] A. Knigavko, B. Rosenstein, and Y.-F. Chen, Magnetic skyrmions and their lattices in triplet superconductors, Phys. Rev. B **60**, 550 (1999).

[29] J. Garaud and E. Babaev, Skyrmionic state and stable half-quantum vortices in chiral $p$-wave superconductors, Phys. Rev. B **86**, 060514(R) (2012).

[30] J. Garaud and E. Babaev, Properties of skyrmions and multi-quanta vortices in chiral $p$-wave superconductors, Sci. Rep. **5**, 17540 (2015).

[31] L.-F. Zhang, V. F. Becerra, L. Covaci, and M. V. Milosevic, Electronic properties of emergent topological defects in chiral $p$-wave superconductivity, Phys. Rev. B **94**, 024520 (2016).

[32] V. F. Becerra, E. Sardella, F. M. Peeters, and M. V. Milosevic, Vortical versus skyrmionic states in mesoscopic $p$-wave superconductors, Phys. Rev. B **93**, 014518 (2016).

[33] N. D. Mermin, The topological theory of defects in ordered media, Rev. Mod. Phys. **51**, 591 (1979).

[34] H.-B. Braun, Topological effects in nanomagnetism: from superparamagnetism to chiral quantum solitons, Adv. Phys. **61**, 1 (2012).

[35] J. Garaud and E. Babaev, Domain walls and their experimental signatures in $s + is$ superconductors, Phys. Rev. Lett. **112**, 017003 (2014).

[36] L.-F. Zhang, Y.-Y. Zhang, G.-Q. Zha, M. V. Milosevic, and S. P. Zhou, Skyrmionic chains and lattices in $s + id$ superconductors, Phys. Rev. B **101**, 064501 (2020).

[37] R.-F. Chai and G.-Q. Zha, Topological defect states and phase transitions in mesoscopic superconducting squares with Rashba spin-orbit interaction, Eur. Phys. J. B **95**, 101 (2022).

[38] G.-Q. Zha, Skyrmionic configuration and half-quantum vortex-antivortex pair in mesoscopic $p$-wave superconducting noncircular systems, Phys. Rev. B **95**, 014510 (2017).

[39] G.-Q. Zha and R.-F. Chai, Topological defect states in mesoscopic superconducting squares with spin correlations, Europhys. Lett. **129**, 27002 (2020).

[40] J. Garaud, J. Carlstrom, E. Babaev, and M. Speight, Chiral $CP^2$ skyrmions in three-band superconductors, Phys. Rev. B **87**, 014507 (2013).

[41] A. A. Zyuzin, J. Garaud, and E. Babaev, Nematic skyrmions in odd-parity superconductors, Phys. Rev. Lett. **119**, 167001 (2017).

[42] M. Speight, T. Winyard, and E. Babaev, Symmetries, length scales, magnetic response, and skyrmion chains in nematic superconductors, Phys. Rev. B **107**, 195204 (2023).

[43] D.-C. Lu, Y.-Y. Lv, J. Li, B.-Y. Zhu, Q.-H. Wang, H.-B. Wang, and P.-H. Wu, Elliptical vortex and oblique vortex lattice in the FeSe superconductor based on the nematicity and mixed superconducting orders, npj Quantum Mater. **3**, 12 (2018).

[44] G.-Q. Zha, Vortical configurations in mesoscopic superconducting square loop with mixed pairing orders, Europhys. Lett. **130**, 67005 (2020).

[45] X. Liu, J. K. Jain, and C.-X. Liu, Long-range spin-triplet helix in proximity induced superconductivity in spin-orbit-coupled systems, Phys. Rev. Lett. **113**, 227002 (2014).

[46] M. Biderang, H. Yavari, M.-H. Zare, P. Thalmeier, and A. Akbari, Edge currents as a probe of the strongly spin-polarized topological noncentrosymmetric superconductors, Phys. Rev. B **98**, 014524 (2018).

[47] B. Scharf, F. Pientka, H. Ren, A. Yacoby, and E. M. Hankiewicz, Tuning topological superconductivity in phase-controlled Josephson junctions with Rashba and Dresselhaus spin-orbit coupling, Phys. Rev. B **99**, 214503 (2019).

[48] N. Sedlmayr, J. M. Aguiar-Hualde, and C. Bena, Majorana bound states in open quasi-one-dimensional and two-dimensional systems with transverse Rashba coupling, Phys. Rev. B **93**, 155425 (2016).

[49] S. Ikegaya, W. B. Rui, D. Manske, and A. P. Schnyder, Tunable Majorana corner modes in noncentrosymmetric superconductors: Tunneling spectroscopy and edge imperfections, Phys. Rev. Res. **3**, 023007 (2021).

[50] B. J. Baelus, K. Kadowaki, and F. M. Peeters, Influence of surface defects on vortex penetration and expulsion in mesoscopic superconductors, Phys. Rev. B **71**, 024514 (2005).

[51] P. G. de Gennes, *Superconductivity of Metals and Alloys* (Addison-Wesley, New York, 1994).

[52] E. Babaev, L. D. Faddeev, and A. J. Niemi, Hidden symmetry and knot solitons in a charged two-condensate Bose system, Phys. Rev. B **65**, 100512(R) (2002).

[53] J. Garaud and E. Babaev, Vortex chains due to nonpairwise interactions and field-induced phase transitions between states with different broken symmetry in superconductors with competing order parameters, Phys. Rev. B **91**, 014510 (2015).

[54] R. Tao, Y.-J. Yan, X. Liu, Z.-W. Wang, Y. Ando, Q.-H. Wang, T. Zhang, and D.-L. Feng, Direct visualization of the nematic superconductivity in $Cu_xBi_2Se_3$, Phys. Rev. X **8**, 041024 (2018).

[55] G.-Q. Zha, H.-W. Zhao, and S.-P. Zhou, Effect of next-nearest-neighbor hopping on the antiferromagnetism and vortex charges in high-temperature superconductors: Numerical solution of the Bogoliubov-de Gennes equations, Phys. Rev. B **76**, 132503 (2007).

[56] Z.-Y. Zhuang and Z. Yan, Toplogical phase transitions and evolution of boundary states induced by Zeeman fields in second-order topological insulators, Front. Phys. **10**, 866347 (2022).

[57] Y. Zhong, Y. Wang, S. Han, Y.-F. Lv, W.-L. Wang, D. Zhang, H. Ding, Y.-M. Zhang, L. Wang, K. He, R. Zhong, J. A. Schneeloch, G.-D. Gu, C.-L. Song, X.-C. Ma, and Q.-K. Xue, Nodeless pairing in superconducting copper-oxide monolayer films on $Bi_2Sr_2CaCu_2O_{8+\delta}$, Sci. Bull. **61**, 1239 (2016).

[58] K. Jiang, X. Wu, J. Hu, and Z. Wang, Nodeless high-Tc superconductivity in the highly overdoped $CuO_2$ monolayer, Phys. Rev. Lett. **121**, 227002 (2018).

[59] W.-C. Lee, S.-C. Zhang, and C. Wu, Pairing state with a time-reversal symmetry breaking in FeAs-based superconductors, Phys. Rev. Lett. **102**, 217002 (2009).

[60] V. Grinenko, P. Materne, R. Sarkar, H. Luetkens, K. Kihou, C. H. Lee, S. Akhmadaliev, D. V. Efremov, S.-L. Drechsler, and H.-H. Klauss, Superconductivity with broken time-reversal symmetry in ion-irradiated $Ba_{0.27}K_{0.73}Fe_2As_2$ single crystals, Phys. Rev. B **95**, 214511 (2017).

[61] T. Golod, A. Iovan, and V. M. Krasnov, Single Abrikosov vortices as quantized information bits, Nat. Commun. **6**, 8628 (2015).

[62] A. M. Black-Schaffer and C. Honerkamp, Chiral $d$-wave superconductivity in doped graphene, J. Phys.: Condens. Matter **26**, 423201 (2014).

[63] J. Garaud, J. Carlstrom, and E. Babaev, Topological solitons in three-band superconductors with broken time reversal symmetry, Phys. Rev. Lett. **107**, 197001 (2011).